# Electron-electron interactions and high-order harmonics in solids

Didarul Alam , <sup>1</sup> Naseem Ud Din , <sup>1</sup> Michael Chini , <sup>1,2</sup> and Volodymyr Turkowski , <sup>1,\*</sup> <sup>1</sup>Department of Physics, University of Central Florida, Orlando, Florida 32816, USA <sup>2</sup>CREOL, the College of Optics and Photonics, University of Central Florida, Orlando, Florida 32816, USA

(Received 26 August 2022; revised 28 October 2022; accepted 29 November 2022; published 14 December 2022)

The generation of high-order harmonics in bulk systems is a young and fast-growing area of research. Beginning in 2011 with the pioneering studies of high-order harmonic generation in bulk dielectrics, significant progress has already been made in understanding the details of the microscopic mechanisms behind this phenomenon, such as the role of intra- and interband polarization, the contribution of the electronic band structure and dipole moments to the harmonic spectrum, and the effects of structural and electronic symmetry. However, the role of electron-electron correlations in the excited system is much less understood. In this work, we study the role of these effects in the high-order harmonic spectrum by using the Time-Dependent Density Functional Theory (TDDFT) approach with the Dynamical Mean-Field Theory (DMFT) exchange-correlation kernel. In this approximation, one takes into account the time-resolved on-site electron-electron interactions. As we demonstrate, the correlation effects significantly affect the high-harmonic spectrum, most importantly through ultrafast modification of the interband polarization of the system.

## DOI: 10.1103/PhysRevB.106.235124

### I. INTRODUCTION

High-order harmonic generation (HHG) from solids is a rapidly growing branch of ultrafast physics. After the phenomenon was first observed in ZnO in 2011 [1] (see also consequent studies of this material in Refs. [2-5]), it was demonstrated that many other systems, such as MgO [6], Si [7] SiO<sub>2</sub> [8], GaSe [9], MoS<sub>2</sub> [10], graphene [11,12], solid Ar and Kr [13], ZnSe [14], and Al<sub>2</sub>O<sub>3</sub> [15] emit high-order harmonic radiation (for an overview, see the recent review [16]). The emitted harmonics can be used to generate isolated attosecond pulses [17], and it is expected that high-order harmonic spectroscopy techniques can be used to study the properties of solids, including band [3,14], measurements of Berry curvature [18], orbital structures [6], the effects of strong electron-electron correlations [19-21] and topological states [22–26].

Naturally, to study the properties of solids, HHG measurements must be closely bound with accurate theoretical analysis to explain and predict experimental data. The Semiconductor Bloch Equations (SBE), which are the oldest and most traditional approach to analyze ultrafast properties of solids [27-30], have been actively applied to study HHG in solids [23,31–33]. However, this approach, similar to other phenomenological approaches [18,34-38], suffers from shortcomings that forbid to accurately study the effects of electron-electron interaction in the HHG. One reason for this is that including higher-order correlation functions, which can be done by generalizing the SBE in the nonequilibrium Green's function formalism, dramatically increases the computational cost. In this case it is difficult to go beyond a

few-band approximation and to extend calculations to long times due to nonlinear and memory effects. Another important shortcoming is the lack of ab initio accuracy. Indeed, it is difficult to incorporate in the effective theory such quantities as spatial inhomogeneity, the microscopic dielectric function, and accurate band structure beyond the quadratic or cosine dispersions.

For these reasons, an approach based on ab initio Density Functional Theory (DFT) is much more attractive: DFT [39,40] is the theory of effective charge density. In DFT, one needs to deal with the three-dimensional (3D) space variable instead of multi-variables of the SBEs and similar approaches. Once one properly chooses the exchangecorrelation (XC) potential, the effects of electron-electron interaction are, in principle, treated exactly (though, in reality only approximate potentials that might give accurate but approximate solutions are available). In the other approaches discussed above these effects are in almost all cases treated in some (often-uncontrollable) perturbationtheory approximation. Static DFT was applied to study HHG in some systems (in the framework of the time-dependent density-matrix formalism; see, e.g., Refs. [41,42]). Unfortunately, static DFT is not capable to reproduce correctly the excited state energies, and thus it is doubtful if it can be accurately applied in this case. Generalizations of DFT on the excited states, specifically the GW+Bethe-Salpeter Equation approach, was also applied to study HHG [43]. However, the computational cost in this case is very large.

In this sense, the time-dependent generalization of DFT [44,45] is the most optimal approach: it correctly reproduces excited states and is computationally much less expensive as compared to the many-body approaches. TDDFT was already applied to study HHG or ultrafast currents in several solid

<sup>\*</sup>Volodymyr.Turkowski@ucf.edu

crystalline solids [46–53]. However, in most cases, the exchange and correlation effects are taken into account at an insufficient level for treating strong correlations, for example by employing adiabatic LDA [54] or modified Becke-Johnson exchange potentials [55,56].

The first study incorporating the effects of strong electronelectron correlations into the mechanism of HHG was described in Ref. [21], where in the TDDFT+U approach was applied to NiO and it was demonstrated that it is important to take into account dynamical modulation (time-dependence) of the local Coulomb repulsion between the electrons. However, it is well known that DFT+U (or its time-dependent equivalent TDDFT+U) is relevant only in the case of very large U's. In the more relevant case of intermediate values of U [of order of the kinetic energy, defined by the width of the valence band(s)] one needs to apply the DFT+DMFT approach [57,58], which takes into account time-resolved local Coulomb interactions between the electrons. From the many-body side, nonequilibrium DMFT has been applied to analyze the HHG spectrum of a Mott insulator [20] and it was shown that these dynamical effects play an important role.

In this work, we apply our recently-developed DMFT-TDDFT approach [59] to analyze the role of the dynamical (time-resolved) correlation effects in the HHG spectrum of solids. We apply the approach to ZnO, probably the most studied material in the case of HHG in solids with a large amount of available experimental and theoretical data on HHG, e.g., analysis of the role of the transition dipole moments modulus and phase (in particular, in the appearance of even harmonics) [32,33] the effects of the carrier-envelope phase and orientation [60], the role of the interband dynamics in mid-infrared laser fields [2], tuning of the HH spectra in solids [61], effects of the reconstruction of the electronic band structure [3] and some other theoretical results [62–64]. However, in all these studies the electron correlation effects were not included. We perform an analysis of the role of these effects by using an adiabatic local XC kernel obtained as described below and changing its value from zero to the value obtained from ab initio calculations (i.e., artificially tuning the strength of the electron-electron correlations). The obtained results may help to shed the light on the role of correlation effects in the electronic and optical properties of strongly correlated materials.

The article is organized in the following order. In Sec. II we have discussed our theoretical models deriving equations to add correlation in HHG. Then, we share our results, by showing first the electronic properties calculation (Sec. III), then the HH spectra considering both the case with no correlation and with correlation (Sec. IV). Finally, we summarize our findings in Sec. V.

## II. DMFT-TDDFT APPROACH

### A. Density-matrix TDDFT

In the DMFT-TDDFT approach one solves the TDDFT Kohn-Sham equation with the XC potential/kernel obtained from the charge susceptibility obtained from the effective Hubbard model (see next Subsection). In detail, let us consider

the TDDFT Kohn-Sham equation:

$$\hat{H}(r,t)\Psi_k^v(r,t) = i\frac{\partial \Psi_k^v(r,t)}{\partial t},\tag{1}$$

where the Hamiltonian has the following form:

$$\hat{H}(r,t) = -\frac{\nabla^2}{2m} + V_{\text{ion}}(r) + V_H[n](r,t) + V_{\text{XC}}[n](r,t) + e\vec{r} \cdot \vec{E}(t),$$
(2)

with the standard notations for the ion,  $V_{\rm ion}(r)$ , Hartree,  $V_H(r,t)=\int \frac{n(r',t)}{|r-r'|} {\rm d} r'$ , and the XC,  $V_{\rm XC}[n](r,t)$ , potentials. In our case, the last term, the external potential, is laser pulse potential with shape

$$\vec{E}(t) = \vec{E}_0 e^{-\frac{t^2}{T_P^2}} \cos(\omega_0 t + \phi), \tag{3}$$

where  $\omega_0$ ,  $\phi$  and  $T_P$  are the pulse frequency, phase and duration, respectively.

Since  $V_H[n](r,t)$  and  $V_{XC}[n](r,t)$  are functionals of density, Eq. (1) is solved self-consistently with the electron number equation:

$$n(r,t) = \sum_{k < k_F} \left| \Psi_k^{v}(r,t) \right|^2, \tag{4}$$

where  $k_F$  is the Fermi wave vector (i.e., this is formally-defined constrain that means that we perform summation over the valence-band (initially occupied) states, since the evolution of the system can be completely described by the time evolution of these states). Density dependence of the XC potential would significantly complicate the numerical analysis, since in this case one would need to include all bands in calculating density (4) (that define XC potential). Fortunately, the XC potential we use is density independent and a finite set of bands can be used. To solve the system (1), (4), we apply the density-matrix formalism (see Ref. [65] for the main details and Refs. [66,67] for some extensions of the approach), where the wave function is expressed in the basis of a physically motivated set of the static (DFT) wave functions  $\psi_k^l(r)$  [see Eq. (14) below]:

$$\Psi_k^v(r,t) = \sum_{l=v,c} c_k^l(t) \psi_k^l(r).$$
 (5)

The number of included valence (v) and conduction (c) bands depends on the pulse frequency and other pulse parameters

Thus, the problem reduces to finding time-dependent coefficients  $c_k^l(t)$ . Substituting Eq. (5) into Eq. (1), multiplying Eq. (1) from the right by  $\psi_k^{m*}(r)$  and integrating over the space coordinates, one gets the equation for these coefficients:

$$i\frac{\partial c_k^m(t)}{\partial t} = \sum_{l=v,c} H_k^{ml}(t)c_k^l(t),\tag{6}$$

where

$$H_k^{\text{ml}}(t) = \int \psi_k^{m*}(r)\hat{H}(r,t)\psi_k^l(r)dr$$
 (7)

are the matrix elements of the Hamiltonian with respect to the static wave functions. Similarly, for the complex conjugated coefficients:

$$i\frac{\partial c_k^{m*}(t)}{\partial t} = -\sum_{l=v,c} c_k^{l*}(t) H_k^{lm}(t). \tag{8}$$

Instead of solving Eq. (6) or Eq. (8), it is more convenient to construct and solve the equations for the density matrix:

$$\rho_k^{\text{lm}}(t) = c_k^l(t)c_k^{m*}(t), \tag{9}$$

since its elements have a clearer physical meaning (diagonal elements; band occupancies, nondiagonal, transition probabilities), which allows one to truncate or to do other approximations in a controllable manner.

One can obtain from Eqs. (6) and (8) the Liouville equation of motion for the density matrix:

$$i\frac{\partial \rho_k^{\text{lm}}(t)}{\partial t} = [H, \rho]^{\text{lm}}(t)$$

$$\equiv \sum_{n} \left( H_k^{\text{ln}}(t) \rho_k^{\text{nm}}(t) - \rho_k^{\text{ln}}(t) H_k^{\text{nm}}(t) \right), \quad (10)$$

which is an equivalent of the KS Eq. (1) in the density matrix approximation. To express the number equation in the terms of density matrix elements, one can write:

$$\begin{split} n(r,t) - n(r,t &= -\infty) \\ &= \sum_{k < k_F} \left| \Psi_k^v(r,t) \right|^2 - \sum_{k < k_F} \left| \Psi_k^v(r,t = -\infty) \right|^2 \\ &= \sum_{k < k_F} \left( \sum_{l} c_k^{l*}(t) \psi_k^{l*}(r) \right) \left( \sum_{m} c_k^m(t) \psi_k^m(r) \right) \\ &- \sum_{k < k_F} \left( \sum_{l} c_k^{l*}(t = -\infty) \psi_k^{l*}(r) \right) \\ &\times \left( \sum_{m} c_k^m(t = -\infty) \psi_k^m(r) \right). \end{split}$$

This gives the number of electron equation in the density matrix representation:

$$n(r,t) - n(r,t = -\infty) = \sum_{k < k_F, \text{lm}} \psi_k^m(r) \psi_k^{l*}(r) (\rho_k^{\text{ml}}(t) - \rho_k^{\text{ml}}(-\infty)).$$
(11)

The system of Eqs. (10), (11) is the density-matrix version of the KS TDDFT Eqs. (1) and (4).

In this work we use the linear response approximation, expanding the XC potential in linear fluctuations of the charge density. It is important to stress that linear approximation does not assume weak correlations: it is defined as the case when the number of excited charges is small compared to the number of electrons in the system (which is the case of the problem considered here).

To derive the density matrix equations in the case of linear response, let us express the Hamiltonian Eq. (2) in the

linear approximation in terms of charge density fluctuations Eq. (11):

$$\hat{H}(r,t) = \hat{H}_0(r) + \delta \hat{H}(r,t), \tag{12}$$

where

$$\hat{H}_0(r) = -\frac{\nabla^2}{2m} + V_{\text{ion}}(r) + V_H[n](r, t = -\infty) + V_{XC}[n](r, t = -\infty),$$
(13)

is the nonperturbed (DFT) Hamiltonian that satisfies

$$\hat{H}_0(r)\psi_{\iota}^m(r) = \varepsilon_{\iota}^m \psi_{\iota}^m(r), \tag{14}$$

and

$$\delta \hat{H}(r,t) = V_H[n](r,t) - V_H[n](r,t = -\infty) + V_{XC}[n](r,t) - V_{XC}[n](r,t = -\infty) + e\vec{r} \cdot \vec{E}(t)$$
(15)

is the time-dependent (fluctuating) part.

The Hamiltonian matrix elements can be also divided into static and time-dependent parts:

$$H_k^{ml}(t) = \int \psi_k^{m*}(r)(\hat{H}_0(r) + \delta \hat{H}(r, t))\psi_k^l(r)dr$$

$$= \varepsilon_k^m \delta^{ml} + \int \psi_k^{m*}(r)\delta V_H(r, t)\psi_k^l(r)dr$$

$$+ \int \psi_k^{m*}(r)\delta V_{XC}(r, t)\psi_k^l(r)dr + \vec{d}_k^{ml} \cdot \vec{E}(t), \quad (16)$$

where

$$\vec{d}_k^{\rm ml} = e \int \psi_k^{m*}(r) \vec{r\psi}_k^l(r) d\mathbf{r}$$
 (17)

are the dipole matrix elements.

In the linear-response approximation,

$$V_{\rm XC}(r,t) = V_{\rm XC}(r,t=-\infty) + \int \int f_{\rm XC}(r,r',t-t') \times \delta n(r',t') dr' dt', \qquad (18)$$

where

$$f_{\rm XC}(r, r', t - t') = \frac{\delta V_{\rm XC}(r, t)}{\delta n(r', t')} \int_{n(r, t) = n(r, t) = -\infty} (19)$$

is the XC kernel (derived in the next Subsection). Using Eqs. (11) and (18) one can show that

$$\int \psi_k^{m*}(r)\delta V_{\text{XC}}(r,t)\psi_k^l(r)d\mathbf{r} = \sum_{q < k_F,a,b} \int_{-\infty}^t \tilde{F}_{\text{kq}}^{\text{mlab}}(t,t') \times \left(\rho_q^{\text{ab}}(t') - \rho_q^{\text{ab}}(-\infty)\right)dt',$$
(20)

where

$$\tilde{F}_{kq}^{\text{mlab}}(t,t') = \iint d\mathbf{r} d\mathbf{r}' \psi_k^{m*}(r) \psi_k^l(r) f_{\text{XC}}(r,r',t,t')$$

$$\times \psi_q^a(r') \psi_q^{b*}(r')$$
(21)

are the matrix elements that describe the effects of retarded e-e interaction.

Similarly, one can obtain the result for the Hartree part,  $\int \psi_k^{m*}(r) \delta V_H(r,t) \psi_k^I(r) d\mathbf{r} = \int \psi_k^{m*}(r) \left[\int \frac{\delta n(r',t)}{|r-r'|} d\mathbf{r}'\right] \psi_k^I(r) d\mathbf{r}$ :

$$\int \psi_k^{m*}(r)\delta V_H(r,t)\psi_k^l(r)d\mathbf{r} = \sum_{q < k_F,a,b} A_{kq}^{\text{mlab}} \left(\rho_q^{\text{ab}}(t) - \rho_q^{\text{ab}}(0)\right),\tag{22}$$

where

$$A_{\text{kq}}^{\text{mlab}} = \int \int d\mathbf{r} d\mathbf{r}' \psi_k^{m*}(r) \psi_k^l(r) \frac{1}{|r - r'|} \psi_q^a(r') \psi_q^{b*}(r'). \tag{23}$$

These results need to be substituted into the Liouville Eq. (10). Before using these equations, one still needs to

find expressions for the dipole moments. To calculate these moments, it is more convenient to use momentum representation. Namely, from the DFT calculations one obtains the dispersion  $\varepsilon_{\vec{k}}^{\lambda}$  and the wave functions  $\psi_{\vec{k}}^{\lambda}(\vec{r})$ . Then, from the Bloch representation of the wave functions  $\psi_{\vec{k}}^{\lambda}(\vec{r}) = e^{i\vec{k}\vec{r}}u_{\vec{k}}^{\lambda}(\vec{r})$  one extracts their periodic (Bloch) parts  $u_{\vec{k}}^{\lambda}(\vec{r})$  that are used to calculate the transition dipole moments:

$$\vec{D}_{\vec{k}}^{\lambda\lambda'} = i \int_{\text{cell}} u_{\vec{k}}^{\lambda*}(\vec{r}) \vec{\nabla}_{\vec{k}} u_{\vec{k}}^{\lambda}(\vec{r}) d\vec{r}. \tag{24}$$

The explicit form of the DMFT-TDDFT Bloch equations we use in this work is

$$i\frac{\partial \rho_{\vec{k}}^{v,c_j}(t)}{\partial t} = \left( \varepsilon_{\vec{k}}^{c_j} - \varepsilon_{\vec{k}}^{v_j} \right) \rho_{\vec{k}}^{v_i c_j}(t) + \vec{E}(t) \sum_{c_i \neq c_j} \left( \vec{D}_{\vec{k}}^{c_i v_j} \rho_{\vec{k}}^{v_i c_j}(t) - \vec{D}_{\vec{k}}^{c_i c_j} \rho_{\vec{k}}^{v_i c_j}(t) \right) + \vec{E}(t) \sum_{v_i \neq v_j} \left( \vec{D}_{\vec{k}}^{v_i v_j} \rho_{\vec{k}}^{v_i c_j}(t) - \vec{D}_{\vec{k}}^{c_i v_j} \rho_{\vec{k}}^{v_i c_j}(t) \right) + \vec{E}(t) \sum_{v_i \neq v_j} \left( \vec{D}_{\vec{k}}^{v_i v_j} \rho_{\vec{k}}^{v_i c_j}(t) - \vec{D}_{\vec{k}}^{c_i v_j} \rho_{\vec{k}}^{v_i v_j}(t) \right) + \vec{E}(t) \sum_{v_i \neq v_j} \left( \vec{D}_{\vec{k}}^{v_i v_j} \rho_{\vec{k}}^{v_i c_j}(t) - \rho_{\vec{k}}^{v_i v_j}(t) \right) + \vec{E}(t) \sum_{c_i \neq c_j} \vec{D}_{\vec{k}}^{c_i c_i} \rho_{\vec{k}}^{v_i c_j}(t) + \vec{E}(t) \sum_{c_i \neq c_j} \vec{D}_{\vec{k}}^{c_i c_i} \rho_{\vec{k}}^{v_i c_j}(t) - \vec{E}(t) \sum_{c_i \neq c_j} \vec{D}_{\vec{k}}^{c_i c_i} \rho_{\vec{k}}^{c_i c_i}(t) + \vec{E}(t) \sum_{v_i} \left( \vec{D}_{\vec{k}}^{v_i v_j} \rho_{\vec{k}}^{v_i c_j}(t) - \rho_{\vec{k}}^{v_i v_i}(t) \right) + \vec{E}(t) \vec{D}_{\vec{k}}^{c_i c_i} \rho_{\vec{k}}^{c_i c_i}(t) + \vec{E}(t) \sum_{c_i \neq c_j} \vec{D}_{\vec{k}}^{c_i c_i} \rho_{\vec{k}}^{c_i c_i}(t) + \vec{E}(t) \sum_{c_i \neq c_j} (\vec{D}_{\vec{k}}^{v_i v_i} \rho_{\vec{k}}^{c_i c_i}(t) - \rho_{\vec{k}}^{c_i v_i}(t) \right) + \vec{E}(t) \vec{D}_{\vec{k}}^{c_i c_i}(t) + \vec{E}(t) \sum_{c_i \neq c_i} \vec{D}_{\vec{k}}^{v_i v_i} \rho_{\vec{k}}^{v_i v_i}(t) - \vec{E}(t) \sum_{c_i \neq c_i} \vec{D}_{\vec{k}}^{v_i v_i} \rho_{\vec{k}}^{v_i v_i}(t) - \rho_{\vec{k}}^{c_i v_i}(t) \right) + \vec{E}(t) \vec{D}_{\vec{k}}^{v_i v_i}(t) + \vec{E}(t) \vec$$

where

$$U_k^{\lambda\lambda'} = \sum_{q < k_F, q, b} \int_0^t F_{kq}^{\lambda\lambda'ab}(t - t') \left(\rho_q^{ab}(t') - \rho_q^{ab}(0)\right) dt'$$
(30)

and

$$F_{\rm kq}^{\rm mlab}(t,t') = \iint {\rm d}r {\rm d}r' \psi_k^{m*}(r) \psi_k^l(r) \left( \frac{1}{|r-r'|} \delta(t,t') + f_{\rm XC}(r,r',t,t') \right) \psi_q^a(r') \psi_q^{b*}(r'). \tag{31}$$

One more, missing, type of matrix element  $\rho_{\vec{k}}^{c_i v_j}(t)$  should not be calculated separately, since by definition  $\rho_{\vec{k}}^{c_i v_j}(t) = \rho_{\vec{k}}^{v_j c_i *}(t)$ .

### B. DMFT XC kernel

To find the expression for  $f_{XC}(r, t; r't')$ , and hence the interaction elements (31), we use Ref. [59] for the Hubbard Hamiltonian for correlated systems:

$$H = -\sum_{i,j,l,m,\sigma} t_{ij,\sigma}^{lm} c_{i\sigma}^{l+} c_{j\sigma}^{m} - \mu \sum_{i,l,\sigma} c_{i\sigma}^{l+} c_{l}^{l} + U \sum_{i,l} n_{i\uparrow}^{l} n_{i\downarrow}^{l}$$

$$+ (U - J) \sum_{i,l \neq m} n_{i\uparrow}^{l} n_{i\downarrow}^{m} + (U - 2J) \sum_{i,l \neq m,\sigma} n_{i\sigma}^{l} n_{i\sigma}^{m}, \quad (32)$$

where  $c^m_{j\sigma}$ ,  $c^{l+}_{i\sigma}$  and  $n^l_{i\sigma}$  are the electron annihilation, creation and number operators with the respective orbital, spin and space indices, nondiagonal  $t^{lm}_{ij,\sigma}$  are the corresponding intersite interorbital hopping parameters and diagonal  $t^{ll}_{ii,\sigma}$  - energy of electron (with minus sign) with spin  $\sigma$  on the orbital l and site i (i, j is the site-, l, m is the orbital, and  $\sigma$  are the spin indices), U is the intraorbital Coulomb repulsion at each site (i.e., when electrons are at the same orbital), U-J and U-2J are the corresponding interorbital (different-orbital electrons), opposite-spin and same-spin Coulomb repulsions (J is the exchange energy parameter), and  $\mu$  is the chemical potential. In our calculations, we use U=4 eV and J=1 eV. Most of the single-particle properties, collective excitations and responses can be obtained from the spin- and orbital-dependent single-particle Green's function

$$G_{\sigma\sigma'}^{ll'}(r,t;r',t') = -\langle \hat{T}c_{\sigma}^{l}(r,t)c_{\sigma'}^{l'+}(r',t')\rangle$$
 (33)

and two-particle susceptibility

$$\chi_{\sigma\sigma'}^{ll'}(r,t;r',t') = -\langle \hat{T}n_{\sigma}^{l}(r,t)n_{\sigma'}^{l'}(r',t')\rangle, \tag{34}$$

where  $\hat{T}$  is the time-ordering operator. In the DMFT approximation, which is usually a very good approximation for bulk systems, only nonlocal-in-time and local-in-space (site-diagonal) electron self-energy is taken into account, which corresponds to taking into account time-resolved local electron-electron interactions, and neglecting nonlocal in-space interactions. The susceptibility (34) can be also used to find the TDDFT XC kernel, through the relationship:

$$\chi(r,t;r',t') = -\langle \hat{T}n(r,t)n(r',t')\rangle = \sum_{l,l',\sigma,\sigma'} \chi_{\sigma\sigma'}^{ll'}(r,t;r',t')$$
(35)

as

$$f_{XC}(r, r', \omega) = \chi_0^{-1}(r, r', \omega) - \chi^{-1}(r, r', \omega) - \frac{1}{|r - r'|}$$
(36)

(in the real frequency representation). In Eq. (36),  $\chi_0^{-1}$  is the inverse susceptibility in the "noninteracting" (DFT) case. Thus, provided the functions  $\chi_{\sigma\sigma'}^{ll'}(r,t;r',t')$  are known, one can find the total-charge XC kernel from Eqs. (35) and (36). In our study, we use iterative perturbation theory approximation to find the Green's function (33) and one-loop approximation to calculate the susceptibility (34).

In our TDDFT calculations, we neglect memory effects. Thus, since the XC is also local in space,

$$f_{XC}(r, r', \omega) = \delta(r - r') \left[ \chi_0^{-1}(\omega) - \chi^{-1}(\omega) \right] - \frac{1}{|r - r'|}$$
(37)

(where we use DMFT, local-in-space and site independent susceptibilities), the matrix elements Eq. (31) become

$$F_{kq}^{\text{mlab}}(t,t') = \delta(t-t')f_{XC}(\omega=0) \int d\mathbf{r} \ \psi_k^{m*}(r)\psi_k^l(r)\psi_q^a$$

$$\times (r)\psi_a^{b*}(r), \tag{38}$$

where  $f_{XC}(\omega = 0) \approx 32.1$  eV. Due to a very high computational (memory) cost (in particular, even to store this matrix one needs several Gbs), for these matrix elements we use the orbital- and momentum averaged value:

$$F_{\rm kq}^{\rm mlab}(t,t') \approx \delta(t-t')G,$$
 (39)

where

$$G = f_{XC}(\omega = 0) \overline{\int dr \ \psi_k^{m*}(r) \psi_k^l(r) \psi_q^a(r) \psi_q^{b*}(r)} \approx \frac{1.5 \text{eV}}{\mathring{A}^3}.$$
(40)

In other words, the "correlation" parameter G is a product of two parts; the XC kernel  $f_{XC}(\omega=0)$  that is defined by the Hubbard model parameters (most importantly, it is proportional to some power of U), and the overlap of localized (d) orbitals through the average  $\int d\mathbf{r} \ \psi_k^{m*}(r) \psi_k^l(r) \psi_q^a(r) \psi_q^{b*}(r)$ . Though there is no direct relation between these two parts, one may expect that they both, and hence G, grow with U increasing (in particular, because stronger localized orbitals give larger overlap integral, and at the same time they correspond to larger U).

Similar to the case of the Green's function, local-in-space approximation for the XC kernel corresponds to neglecting nonlocal-in-space interactions, which are less important than local ones for extended correlated systems. Adiabatic approximation for the kernel is expected to be an accurate approximation for the dynamics that extends beyond 1–20 fs (when, e.g., time dependence of the local repulsion plays an important role [21], which is the case we study, since our pulse is much longer than 20 fs and we expect memory should not play a significant role in the HH spectrum.

To explore the role of correlation effects, we will perform calculations by changing G from 0 to its actual value  $G \approx 1.5$ . The physical meaning of the coefficient G is the averaged-over-orbitals overlap of the interacting on-site charges. While in ZnO this overlap is not extremely large, in transition-metal oxides and other materials where electron correlations are much more pronounced, the value of G is an order of magnitude larger.

### C. High-order harmonic generation

Once the TDDFT problem Eqs. (25)–(29) is solved, the HHG spectrum can be calculated:

$$S_{\rm HHG}(\omega) = |\hat{\varepsilon}. \int_{-\infty}^{\infty} [\vec{J}_{\rm intra}(t) + \vec{J}_{\rm inter}(t)] e^{i\omega t} dt|^{2}, \qquad (41)$$

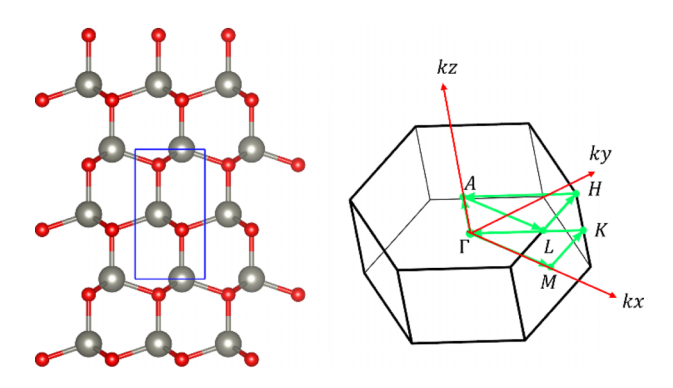


FIG. 1. Left: ZnO (wurtzite) unit cell used in the calculations. The grey and the red balls are the Zn and O atoms, respectively. Right: the Brillouin zone and the high symmetry points.

where  $\hat{\varepsilon}$  is the pulse polarization,

$$\vec{J}_{\text{intra}}(t) = \sum_{\lambda = c, \nu} \int_{\text{BZ}} \vec{v}_{\vec{k}}^{\lambda} \rho_{\vec{k}}^{\lambda}(t) d\vec{k}$$
 (42)

is the intraband and

$$\vec{j}_{inter}(t) = \frac{\partial \vec{P}_{inter}(t)}{\partial t}$$
 (43)

is the interband current, and

$$\vec{P}_{\text{inter}}(t) = \sum_{\lambda,\lambda'} \int_{\text{BZ}} \left[ \vec{D}_{\vec{k}}^{\lambda\lambda'}(\vec{k}) \rho_{\vec{k}}^{\lambda\lambda'}(t) + \text{c.c.} \right] d\vec{k}$$
 (44)

is the interband polarization.

In. Eq. (38),  $\vec{v}_{\vec{k}}^{\lambda} = \frac{\partial \varepsilon_{\vec{k}}^{\lambda}}{\partial \vec{k}}$  is the band dispersion.

### III. ELECTRONIC PROPERTIES: DFT RESULTS

The DFT and DFT+U calculations were performed using the QUANTUM ESPRESSO code [68,69] with norm-conserving pseudopotentials, PBE XC potential [70], the energy cutoff 60 Ry and  $11 \times 11 \times 11$  k points in the Brillouin zone. The unit cell of the systems and the Brillouin zone used in the calculations are shown in Fig. 1.

The calculated DFT band structure of the system is shown in the top left Fig. 2. The spectrum shows the direct bandgap at the  $\gamma$  point, with strongly underestimated value (0.7 eV) as compared to the experimental result of 3.3 eV. In our

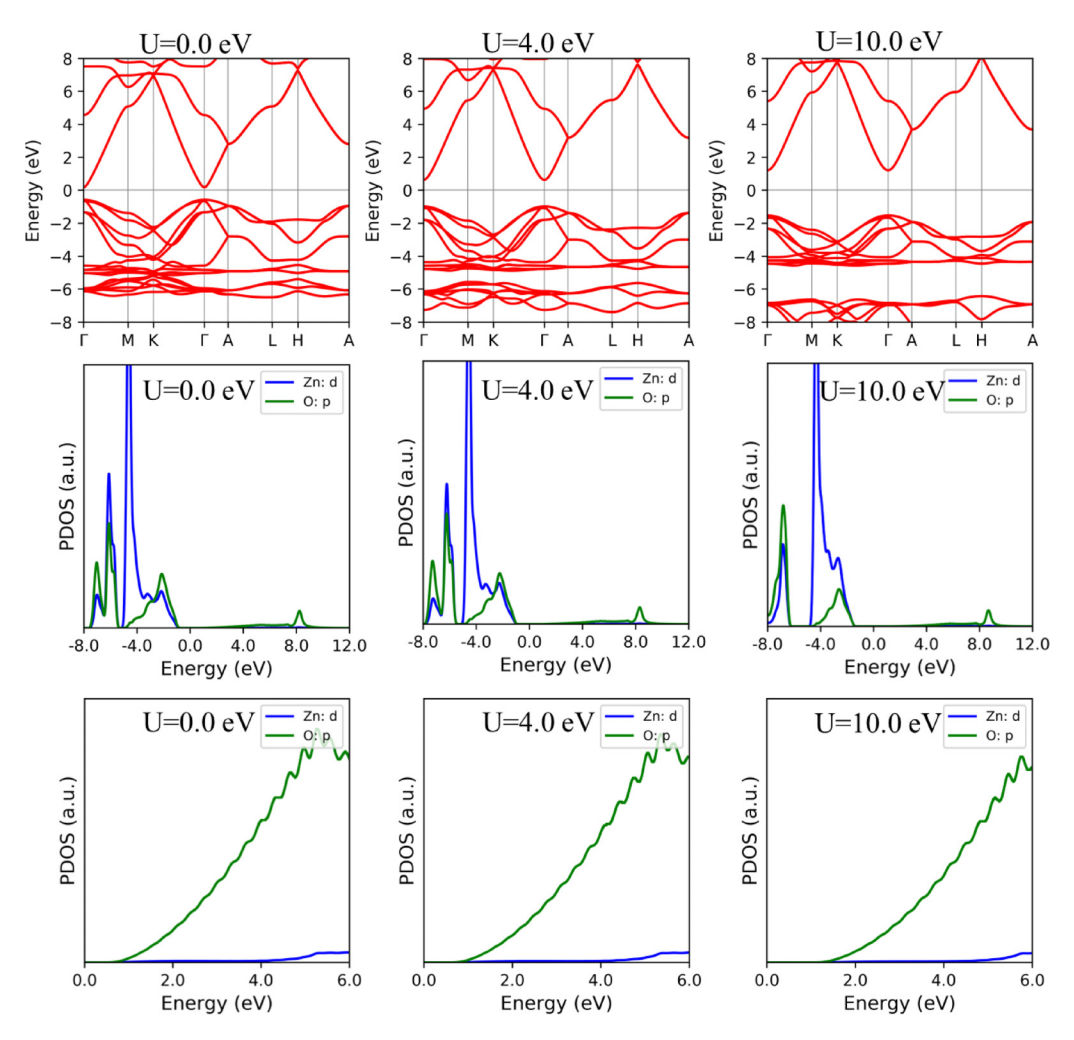


FIG. 2. Top: The band structure of the system obtained with DFT calculations for U = 0, 4 and 10 eV respectively and the Fermi energy is at 0 eV. Middle: The DOS of ZnO and Bottom: The DOS above the fermi label.

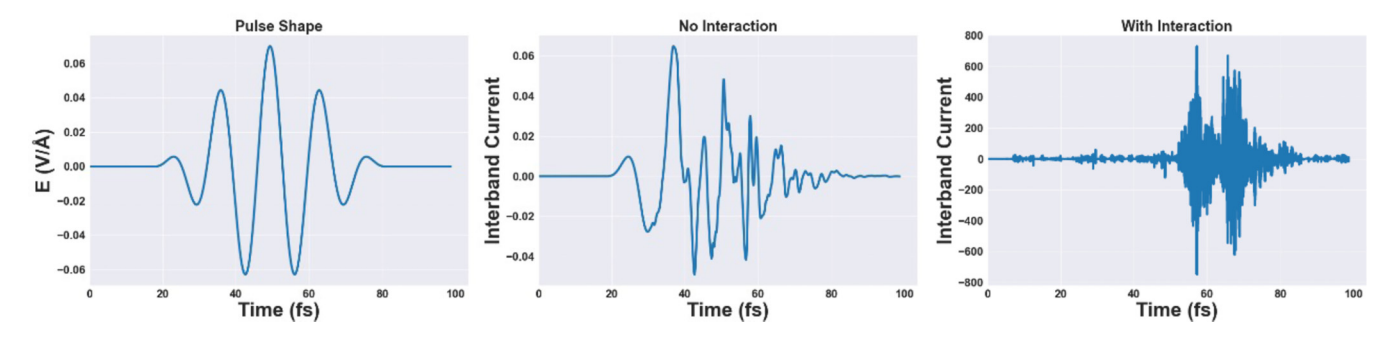


FIG. 3. The pulse (left) and the interband current in the cases of no correlations (middle) and when correlations are taken into account (right, G = 1.5).

DMFT-TDDFT calculations, we apply the scissors procedure by shifting the bandgap to the experimental value. It is important to note that one can obtain the correct gap when one applies the DFT+U approach, though values of U usually used in the DFT+U calculations (as summarized, e.g., in a recent review by Harun et al. [71] are unphysically large, 10-15 eV. We have performed DFT+U calculations of the band structure and projected density of states (DOS) at different values of U (Fig. 2). As it follows from our results, indeed the gap increases with increasing value of U. It is very important that the shape of the bands (at least the ones we used in our TDDFT analysis) changes very weakly. Another important result is that we also did not find a significant change in the hybridization of the valence and conduction Zn-d and O-p orbitals as U increased from 0 to used in this work 4 eV (middle and bottom Fig. 2; see also work by Yaakob et al. [72], where a similar trend was found). Thus, our input DFT band structure with scissor-shifted bandgap is basically equivalent to the DFT+U input for the TDDFT calculations (Another reason that constrained us from using the DFT+U input is difficulties in getting the DFT+U static wave functions with OUANTUM ESPRESSO to calculate interaction parameter G (see below); though, we expect that they should be, similar to the band structure, rather similar to the DFT ones).

The atom- and orbital-resolved DOS of the system is shown in the right Fig. 2. As it follows from the results of our calculations, the top valence band is predominantly of the O-p

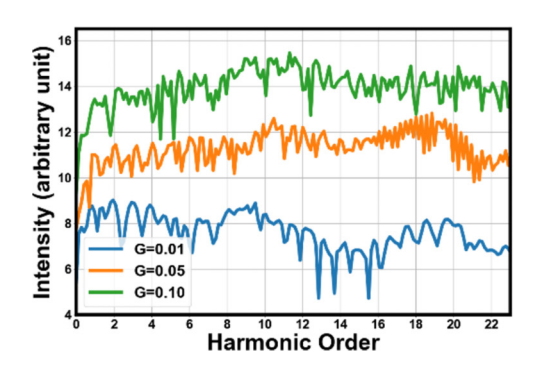
states, while the bottom conduction band states consist of O-p and several Zn orbital states, with dominant Zn-s contribution.

Using the obtained DFT electronic structure and the XC kernel that describes correlation effects we analyzed the HH spectrum of the system.

#### IV. HHG in ZnO

### A. Current

To analyze the role of correlations in the response of the system we begin with the calculation of the dominating interband current Eq. (43) at different correlation strengths, i.e., different values of G (it must be noted that, as theoretical studies show, the relative contribution of the intra- and interband processes in the HH spectrum depends on systems, e.g., in MoS<sub>2</sub> the intra-band currents play a more important role [42], in  $\alpha$ -quartz, the interband ones [48], while in Si coupled intra- and interband dynamics is important [50]. The results for the pulse with parameters, pulse duration  $\sim$ 33 fs, field strength  $E_0 = 0.07 \, \text{V/Å}$  and pulse frequency  $\omega_0 =$ 0.3 eV, are shown in Fig. 3 (unless specified, we use these parameters throughout the paper). In our calculations, we included two valence and two conduction bands and use constant (momentum-independent, with modulus equal 1) dipole moments. As it follows from Fig. 3, the nonlinear effects, evident from high-frequency oscillations in the interband current, grow with increasing correlations. The time dependence of the components of the current strongly depends on the value



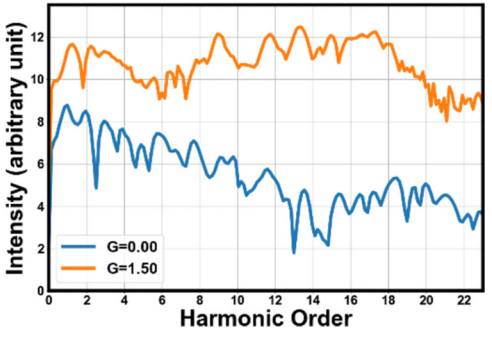
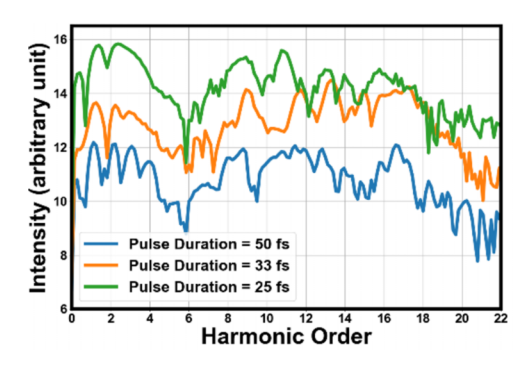


FIG. 4. Interband high harmonic spectrum for different strengths of correlations (For better visual clarity, each curve is normalized individually). Pulse parameters – pulse duration  $\sim 33$  fs, field strength  $E_0 = 0.07$  V/Å and pulse frequency  $\omega_0 = 0.3$  eV.



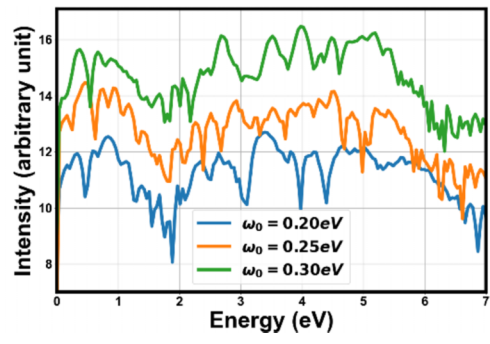


FIG. 5. Comparing HH spectrum for different values of pulse duration at  $E_0 = 0.07 \text{ V/Å}$ ,  $\omega_0 = 0.3 \text{ eV}$ . (left) and for different values of the laser-pulse frequency at pulse duration  $\sim 33 \text{ fs}$  and  $E_0 = 0.07 \text{ V/Å}$  (right) in the case of correlations.

of G, becoming more nonlinear as  $G \sim U^2$  increases. As a result, one can expect emissions at high photon energies when correlations are taken into account.

#### B. HH spectrum

Indeed, our results for the (interband response) HH spectrum at different G's (pulse parameters defined in the previous subsection, out-of-plane perturbation) shown in left Fig. 4 demonstrate that with the increase of correlations the harmonic cutoff (the highest photon energy of the emission) extends to higher photon energies. Importantly, the harmonics spectral weight shifts to higher frequencies with increasing G, similar to the results obtained for the 1D Fermi-Hubbard model [19]. This can be easily seen from right Fig. 4. The reason for the growing number of harmonics is new excited states with energy  $\sim U$ , created by correlations (U is the energy of an electron when the second electron is present at the same site). The energy of these states increases with U, thus resulting in higher-frequency transitions, and hence, in emission with high-order harmonics. In addition, the HH cutoff energy in the case of no interaction is around the 12<sup>th</sup> harmonic (3.6 eV) and in the interaction case, around the 18th harmonic (5.4 eV). Therefore, correlations increase the cutoff energy of the HH spectrum.

In Fig. 5, we demonstrate the effects of pulse duration and laser pulse frequency on HHG in the case when correlations are present. On the left Fig. 5 (pulse duration dependence), the pulse parameters are: the field strength  $E_0 = 0.07 \text{ V/Å}$ , G = 1.5,  $\omega_0 = 0.3 \text{ eV}$ . For all values of the duration of the pulse the cutoff value for the order of harmonic was found to be around 18 (energy  $\sim 5.4 \text{ eV}$ ). On the other hand, in the case of long pulse duration, we have found that below-gap harmonics have more discrete harmonic frequencies (e.g., for 50 fs one can see clear peaks corresponding to the 2nd, 3rd, and 4th, harmonics, while for 33 and 25 fs these are smeared out).

The dependence of the HH spectrum on pulse frequency was analyzed for frequencies  $\omega_0 = 0.2, 0.25$ , and  $0.3 \, \text{eV}$  (right Fig. 5). For  $\omega_0 = 0.2 \, \text{eV}$  the spectrum cut-off energy was found to be around 6 eV, while for both  $\omega_0 = 0.25 \, \text{eV}$  and  $\omega_0 = 0.3 \, \text{eV}$  it is around 5.4 eV. The extension of the harmonic cutoff for lower driving frequencies indicates that obtained nonlinear response cannot be described perturba-

tively. A similar dependence of the spectrum on frequency was found theoretically in diamond [51].

The dependence of the HH spectrum on the strength of the pulse field is shown in Fig. 6. We found a quasilinear relation between the field strength and the spectrum cut-off energy. An increase in the number of harmonics with field increase is expected, since in the more nonlinear case more electrons are excited and correlations are more pronounced. A similar result was obtained in the case of the Hubbard model solved with nonequilibrium DMFT [20]. In general, as our analysis shows, the dependence of the spectrum on the pulse parameters is rather similar in the noninteracting (not shown) and interacting cases, though the emission intensity is stronger in the interacting case.

Finally, in order to analyze the role of the number of the bands involved in the dynamics, we performed calculations in the case of a smaller number of bands; one valence and one conduction band. As it follows from our calculations, in the case of two bands the HH spectrum depends more weakly on the strength of correlations (left Fig. 7) compared to two valence and two conduction bands (right Fig. 7). Thus, correlation effects (electron-scattering) play a more important role when a large number of bands are optically excited. The reason for this is a larger number of excited and dynamically interacting (moving to different sites) charges when the number of bands is larger, thus the interacting terms in the TDDFT equations [proportional to matrix elements F, Eq. (31)] become larger when the number of bands increases.

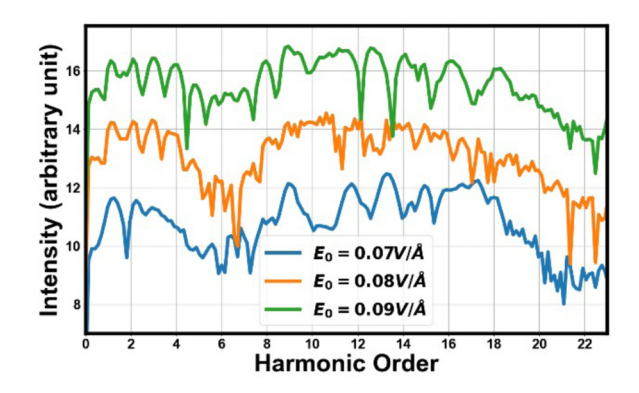
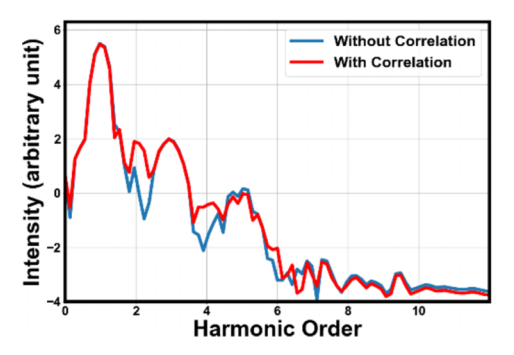


FIG. 6. HH spectrum for different values of the field strength at pulse duration  $\sim 33$  fs and  $\omega_0 = 0.3$  eV in the case of correlations.



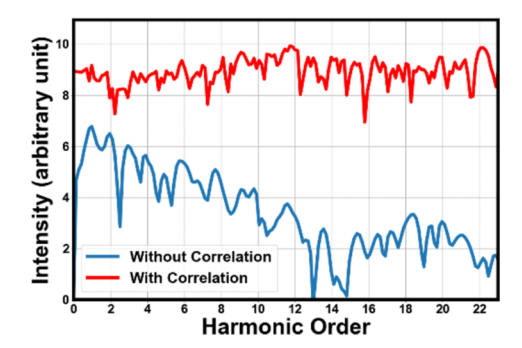


FIG. 7. HH spectrum for the case of one valence and one conduction band (left) and two valence and two conduction bands (right) with and without correlation effects. Pulse parameters – pulse duration  $\sim 33$  fs, field strength  $E_0 = 0.07$  V/Å and pulse frequency  $\omega_0 = 0.3$  eV.

### V. CONCLUSIONS

We have generalized the DMFT-TDDFT approach [59] in the case of HHG and other nonlinear optical effects in materials where electron-electron correlations play an important role. We applied the approach to analyze the effects of electron interaction in the HH spectrum of ZnO, probably the most studied material in the case of HHG in solids. We have found that interband currents, proportional to the time-derivative of the interband polarization, give dominating contribution to the HH spectrum, and this polarization strongly depends on the strength of correlation effects. It is demonstrated that correlation effects shift the peak of the HH spectrum to higher-order harmonics, with the center-ofmass of the spectrum at harmonic number  $n \sim U/\omega_0$ . The number of harmonics dramatically increases with the increase of the strength of correlations and the number of optically excited bands. While the exact value of U in this system is not known, these results show that correlation effects are expected to increase the number of harmonics and move the spectrum in the ultraviolet direction. Also, as we found, while the HH spectrum significantly depends on the value of some of the pulse parameters, like the frequency  $\omega_0$  and  $E_0$ , it is much less sensitive to the value of the pulse duration. Thus, we have developed a methodology to study the effects of strong electron-electron correlations on the optical response of correlated materials and applied it to ZnO. We expect the general trends of the found correlation effect, like a larger of the number of harmonics in systems with larger U and enhancement of the role of the correlation effects in the case of stronger pulses (when a larger number of bands are involved in the dynamics), will hold for other materials as well.

### **ACKNOWLEDGMENTS**

We thank S. Gholam-Mirzaei for numerous enlightening discussions. We thank the UCF Stokes Advanced Research Computing Center for the use of its computational resources. This research was supported by the United States National Science Foundation (NSF) under Grant No. DMR-1809181 and by the AFOSR under Grant No. FA9550-20-1-0284.

- [1] S. Ghimire, A. D. DiChiara, E. Sistrunk, P. Agostini, L. F. DiMauro, and D. A. Reis, Observation of high-order harmonic generation in a bulk crystal, Nat. Phys. 7, 138 (2011).
- [2] G. Vampa, T. J. Hammond, N. Thiré, B. E. Schmidt, F. Légaré, C. R. McDonald, T. Brabec, and P. B. Corkum, Linking high harmonics from gases and solids, Nature (London) 522, 7557 (2015).
- [3] G. Vampa, T. J. Hammond, N. Thiré, B. E. Schmidt, F. Légaré, C. R. McDonald, T. Brabec, D. D. Klug, and P. B. Corkum, All-Optical Reconstruction of Crystal Band Structure, Phys. Rev. Lett. 115, 193603 (2015).
- [4] S. Gholam-Mirzaei, J. Beetar, and M. Chini, High harmonic generation in ZnO with a high-power Mid-IR OPA, Appl. Phys. Lett. **110**, 061101 (2017).
- [5] Z. Wang, H. Park, Y. H. Lai, J. Xu, C. I. Blaga, F. Yang, P. Agostini, and L. F. DiMauro, The roles of photo-carrier doping and driving wavelength in high harmonic generation from a semiconductor, Nat. Commun. 8, 1686 (2017).
- [6] Y. S. You *et al.*, Laser waveform control of extreme ultraviolet high harmonics from solids, Opt. Lett. 42, 1816 (2017).

- [7] G. Vampa *et al.*, Strong-field optoelectronics in solids, Nat. Photonics **12**, 465 (2018).
- [8] T. T. Luu, M. Garg, S. Y. Kruchinin, A. Moulet, M. T. Hassan, and E. Goulielmakis, Extreme ultraviolet high-harmonic spectroscopy of solids, Nature (London) 521, 7553 (2015).
- [9] O. Schubert *et al.*, Sub-cycle control of terahertz high-harmonic generation by dynamical bloch oscillations, Nat. Photonics 8, 119 (2014).
- [10] H. Liu, Y. Li, Y. S. You, S. Ghimire, T. F. Heinz, and D. A. Reis, High-harmonic generation from an atomically thin semiconductor, Nat. Phys. 13, 262 (2017).
- [11] N. Yoshikawa, T. Tamaya, and K. Tanaka, High-harmonic generation in graphene enhanced by elliptically polarized light excitation, Science **356**, 736 (2017).
- [12] H. A. Hafez *et al.*, Extremely efficient terahertz high-harmonic generation in graphene by hot dirac fermions, Nature (London) 561, 7724 (2018).
- [13] G. Ndabashimiye, S. Ghimire, M. Wu, D. A. Browne, K. J. Schafer, M. B. Gaarde, and D. A. Reis, Solid-state

- harmonics beyond the atomic limit, Nature (London) **534**, 7608 (2016).
- [14] A. A. Lanin, E. A. Stepanov, A. B. Fedotov, and A. M. Zheltikov, Mapping the electron band structure by intraband high-harmonic generation in solids, Optica 4, 516 (2017).
- [15] H. Kim, S. Han, Y. W. Kim, S. Kim, and S.-W. Kim, Generation of coherent extreme-ultraviolet radiation from bulk sapphire crystal, ACS Photonics 4, 1627 (2017).
- [16] S. Ghimire and D. A. Reis, High-harmonic generation from solids, Nat. Phys. 15, 10 (2019).
- [17] M. Garg, M. Zhan, T. T. Luu, H. Lakhotia, T. Klostermann, A. Guggenmos, and E. Goulielmakis, Multi-petahertz electronic metrology, Nature (London) 538, 7625 (2016).
- [18] T. T. Luu and H. J. Wörner, Measurement of the berry curvature of solids using high-harmonic spectroscopy, Nat. Commun. 9, 916 (2018).
- [19] R. E. F. Silva, I. V. Blinov, A. N. Rubtsov, O. Smirnova, and M. Ivanov, High-harmonic spectroscopy of ultrafast many-body dynamics in strongly correlated systems, Nat. Photonics 12, 266 (2018).
- [20] Y. Murakami, M. Eckstein, and P. Werner, High-Harmonic Generation in Mott Insulators, Phys. Rev. Lett. 121, 057405 (2018).
- [21] N. Tancogne-Dejean, M. A. Sentef, and A. Rubio, Ultrafast Modification of Hubbard U in a Strongly Correlated Material: *Ab Initio* High-Harmonic Generation in Nio, Phys. Rev. Lett. **121**, 097402 (2018).
- [22] D. Bauer and K. K. Hansen, High-Harmonic Generation in Solids with and without Topological Edge States, Phys. Rev. Lett. **120**, 177401 (2018).
- [23] A. Chacón *et al.*, Circular dichroism in higher-order harmonic generation: Heralding topological phases and transitions in chern insulators, Phys. Rev. B **102**, 134115 (2020).
- [24] Y. Bai, F. Fei, S. Wang, N. Li, X. Li, F. Song, R. Li, Z. Xu, and P. Liu, High-harmonic generation from topological surface states, Nat. Phys. 17, 311 (2021).
- [25] D. Baykusheva *et al.*, All-optical probe of three-dimensional topological insulators based on high-harmonic generation by circularly polarized laser fields, Nano Lett. **21**, 8970 (2021).
- [26] C. Heide *et al.*, Probing topological phase transitions using high-harmonic generation, Nat. Photonics **16**, 620 (2022).
- [27] H. Haug and S. W. Koch, *Quantum Theory of the Optical and Electronic Properties of Semiconductors*, 5th ed. (World Scientific, Singapore, 2009).
- [28] J. F. Müller, R. Mewis, and H. Haug, Theory of the nonlinear optical polarization in laser-excited semiconductors, Z. Für Phys. B Condens. Matter 69, 231 (1987).
- [29] S. Schmitt-Rink, D. S. Chemla, and H. Haug, Nonequilibrium theory of the optical stark effect and spectral hole burning in semiconductors, Phys. Rev. B **37**, 941 (1988).
- [30] M. Lindberg and S. W. Koch, Effective bloch equations for semiconductors, Phys. Rev. B 38, 3342 (1988).
- [31] T. T. Luu and H. J. Wörner, High-order harmonic generation in solids: A unifying approach, Phys. Rev. B **94**, 115164 (2016).
- [32] S. Jiang, H. Wei, J. Chen, C. Yu, R. Lu, and C. D. Lin, Effect of transition dipole phase on high-order-harmonic generation in solid materials, Phys. Rev. A **96**, 053850 (2017).
- [33] S. Jiang, J. Chen, H. Wei, C. Yu, R. Lu, and C. D. Lin, Role of the Transition Dipole Amplitude and Phase on the Generation of Odd and Even High-Order Harmonics in Crystals, Phys. Rev. Lett. 120, 253201 (2018).

- [34] I. N. Ansari, M. S. Mrudul, M. F. Ciappina, M. Lewenstein, and G. Dixit, Simultaneous control of harmonic yield and energy cutoff of high-order harmonic generation using seeded plasmonically enhanced fields, Phys. Rev. A 98, 063406 (2018).
- [35] E. Drobnyh, R. Pachter, and M. Sukharev, Harmonic generation by metal nanostructures optically coupled to two-dimensional transition-metal dichalcogenide, J. Phys. Chem. C 123, 6898 (2019).
- [36] T. N. Ikeda, K. Chinzei, and H. Tsunetsugu, Floquet-theoretical formulation and analysis of high-order harmonic generation in solids, Phys. Rev. A 98, 063426 (2018).
- [37] G.-R. Jia, X.-Q. Wang, T.-Y. Du, X.-H. Huang, and X.-B. Bian, High-order harmonic generation from 2d periodic potentials in circularly and bichromatic circularly polarized laser fields, J. Chem. Phys. 149, 154304 (2018).
- [38] H. K. Avetissian and G. F. Mkrtchian, Higher harmonic generation by massive carriers in buckled two-dimensional hexagonal nanostructures, Phys. Rev. B 99, 085432 (2019).
- [39] P. Hohenberg and W. Kohn, Inhomogeneous electron gas, Phys. Rev. 136, B864 (1964).
- [40] W. Kohn and L. J. Sham, Self-consistent equations including exchange and correlation effects, Phys. Rev. 140, A1133 (1965)
- [41] G. P. Zhang, M. S. Si, M. Murakami, Y. H. Bai, and T. F. George, Generating high-order optical and spin harmonics from ferromagnetic monolayers, Nat. Commun. 9, 3031 (2018).
- [42] M.-X. Guan, C. Lian, S.-Q. Hu, H. Liu, S.-J. Zhang, J. Zhang, and S. Meng, Cooperative evolution of intraband and interband excitations for high-harmonic generation in strained MoS<sub>2</sub>, Phys. Rev. B **99**, 184306 (2019).
- [43] C. Attaccalite, M. Palummo, E. Cannuccia, and M. Grüning, Second-harmonic generation in single-layer monochalcogenides: A response from first-principles real-time simulations, Phys. Rev. Mater. 3, 074003 (2019).
- [44] E. Runge and E. K. U. Gross, Density-Functional Theory for Time-Dependent Systems, Phys. Rev. Lett. **52**, 997 (1984).
- [45] C. A. Ullrich, *Time-Dependent Density-Functional Theory:* Concepts and Applications (Oxford University Press, Oxford, 2011).
- [46] S. A. Sato, K. Yabana, Y. Shinohara, T. Otobe, K.-M. Lee, and G. F. Bertsch, Time-dependent density functional theory of high-intensity short-pulse laser irradiation on insulators, Phys. Rev. B 92, 205413 (2015).
- [47] G. Wachter, S. A. Sato, I. Floss, C. Lemell, X.-M. Tong, K. Yabana, and J. Burgdörfer, Controlling ultrafast currents by the nonlinear photogalvanic effect, New J. Phys. 17, 123026 (2015).
- [48] T. Otobe, High-harmonic generation in  $\alpha$ -quartz by electronhole recombination, Phys. Rev. B **94**, 235152 (2016).
- [49] N. Tancogne-Dejean, O. D. Mücke, F. X. Kärtner, and A. Rubio, Impact of the Electronic Band Structure in High-Harmonic Generation Spectra of Solids, Phys. Rev. Lett. 118, 087403 (2017).
- [50] N. Tancogne-Dejean, O. D. Mücke, F. X. Kärtner, and A. Rubio, Ellipticity dependence of high-harmonic generation in solids originating from coupled intraband and interband dynamics, Nat. Commun. 8, 745 (2017).
- [51] I. Floss, C. Lemell, G. Wachter, V. Smejkal, S. A. Sato, X.-M. Tong, K. Yabana, and J. Burgdörfer, Ab initio multiscale

- simulation of high-order harmonic generation in solids, Phys. Rev. A **97**, 011401(R) (2018).
- [52] G. Le Breton, A. Rubio, and N. Tancogne-Dejean, High-harmonic generation from few-layer hexagonal boron nitride: evolution from monolayer to bulk response, Phys. Rev. B 98, 165308 (2018).
- [53] N. Tancogne-Dejean and A. Rubio, Atomic-like high-harmonic generation from two-dimensional materials, Sci. Adv. 4, eaao5207 (2018).
- [54] G. Onida, L. Reining, and A. Rubio, Electronic excitations: Density-functional versus many-body green's-function approaches, Rev. Mod. Phys. 74, 601 (2002).
- [55] A. D. Becke and E. R. Johnson, A simple effective potential for exchange, J. Chem. Phys. 124, 221101 (2006).
- [56] F. Tran and P. Blaha, Accurate Band Gaps of Semiconductors and Insulators with a Semilocal Exchange-Correlation Potential, Phys. Rev. Lett. 102, 226401 (2009).
- [57] G. Kotliar, S. Y. Savrasov, K. Haule, V. S. Oudovenko, O. Parcollet, and C. A. Marianetti, Electronic structure calculations with dynamical mean-field theory, Rev. Mod. Phys. 78, 865 (2006).
- [58] K. Held, I. A. Nekrasov, G. Keller, V. Eyert, N. Blümer, A. K. McMahan, R. T. Scalettar, T. Pruschke, V. I. Anisimov, and D. Vollhardt, Realistic investigations of correlated electron systems with LDA + DMFT, Phys. Status Solidi B 243, 2599 (2006).
- [59] V. Turkowski and T. S. Rahman, Nonadiabatic exchangecorrelation kernel for strongly correlated materials, J. Phys. Condens. Matter 29, 455601 (2017).
- [60] S. Jiang, S. Gholam-Mirzaei, E. Crites, J. E. Beetar, M. Singh, R. Lu, M. Chini, and C. D. Lin, Crystal symmetry and polarization of high-order harmonics in ZnO, J. Phys. B 52, 225601 (2019).
- [61] M. Sivis, M. Taucer, G. Vampa, K. Johnston, A. Staudte, A. Y. Naumov, D. M. Villeneuve, C. Ropers, and P. B. Corkum, Tailored semiconductors for high-harmonic optoelectronics, Science 357, 303 (2017).

- [62] G. Vampa, C. R. McDonald, G. Orlando, D. D. Klug, P. B. Corkum, and T. Brabec, Theoretical Analysis of High-Harmonic Generation in Solids, Phys. Rev. Lett. 113, 073901 (2014).
- [63] G. Vampa, C. R. McDonald, G. Orlando, P. B. Corkum, and T. Brabec, Semiclassical analysis of high harmonic generation in bulk crystals, Phys. Rev. B 91, 064302 (2015).
- [64] C. R. McDonald, G. Vampa, P. B. Corkum, and T. Brabec, Interband bloch oscillation mechanism for high-harmonic generation in semiconductor crystals, Phys. Rev. A 92, 033845 (2015).
- [65] V. Turkowski and C. A. Ullrich, Time-dependent densityfunctional theory for ultrafast interband excitations, Phys. Rev. B 77, 075204 (2008).
- [66] V. Turkowski and M. N. Leuenberger, Time-dependent densityfunctional theory of exciton-exciton correlations in the nonlinear optical response, Phys. Rev. B 89, 075309 (2014).
- [67] V. Turkowski, N. U. Din, and T. S. Rahman, Time-dependent density-functional theory and excitons in bulk and twodimensional semiconductors, Computation 5, 39 (2017).
- [68] P. Giannozzi, QUANTUM ESPRESSO: A modular and open-source software project for quantum simulations of materials, J. Phys. Condens. Matter 21, 395502 (2009).
- [69] P. Giannozzi, Advanced capabilities for materials modelling with QUANTUM ESPRESSO, J. Phys. Condens. Matter 29, 465901 (2017).
- [70] J. P. Perdew, K. Burke, and M. Ernzerhof, Generalized Gradient Approximation Made Simple, Phys. Rev. Lett. 77, 3865 (1996).
- [71] K. Harun, N. A. Salleh, B. Deghfel, M. K. Yaakob, and A. A. Mohamad, DFT + U calculations for electronic, structural, and optical properties of ZnO wurtzite structure: A review, Results Phys. 16, 102829 (2020).
- [72] M. K. Yaakob, N. H. Hussin, M. F. M. Taib, T. I. T. Kudin, O. H. Hassan, A. M. M. Ali, and M. Z. A. Yahya, First principles LDA+U calculations for ZnO materials, Integr. Ferroelectr. 155, 15 (2014).